

Time-Resolved Thickness and Shape-Change Quantification using a Dual-Band Nanoplasmonic Ruler with Sub-Nanometer Resolution

Ferry Nugroho

Vrije Universiteit Amsterdam <https://orcid.org/0000-0001-5571-0454>

Dominika Switlik

University of Warsaw <https://orcid.org/0000-0002-8007-2105>

Antonius Armanious

ETH Zurich <https://orcid.org/0000-0002-8809-4659>

Padraic O'Reilly

Molecular Vista (United States)

Iwan Darmadi

Chalmers University of Technology <https://orcid.org/0000-0002-5921-9336>

Sara Nilsson

Chalmers University of Technology

Vladimir Zhdanov

Chalmers University of Technology

Fredrik Höök

Chalmers

Tomasz Antosiewicz

University of Warsaw <https://orcid.org/0000-0003-2535-4174>

Christoph Langhammer (✉ clangham@chalmers.se)

Chalmers University of Technology <https://orcid.org/0000-0003-2180-1379>

Article

Keywords:

Posted Date: January 20th, 2022

DOI: <https://doi.org/10.21203/rs.3.rs-1169581/v1>

License:   This work is licensed under a Creative Commons Attribution 4.0 International License.

[Read Full License](#)

Abstract

Time-resolved measurements of changes in size and shape of nanobiological objects and layers are crucial to understand their properties and optimize their performance. Optical sensing is particularly attractive with high throughput and sensitivity, and label-free operation. However, most state-of-the-art solutions require intricate modelling or multiparameter measurements to disentangle conformational or thickness changes of biomolecular layers from complex interfacial refractive index variations. Here, we present a dual-band nanoplasmonic ruler comprising mixed arrays of plasmonic nanoparticles with spectrally separated resonance peaks. As electrodynamic simulations and model experiments show, it enables real-time simultaneous measurements of thickness and refractive index variations in uniform and heterogeneous layers with sub-nanometer resolution. Additionally, nanostructure shape changes can be tracked, as demonstrated by quantifying the degree of lipid vesicle deformation at the critical coverage prior to rupture and supported lipid bilayer formation. In a broader context, the presented nanofabrication approach opens the door to multimodal nanoplasmonic optical sensing.

Main

The ability to accurately measure the size and shape of nanoscale objects is one of the key achievements of nanoscience and nanotechnology, since these characteristics dictates many properties and functionalities of nanoscale objects in materials and life science.¹⁻⁴ In the latter area, precise characterization of nanoscopic biological entities is especially important, *e.g.*, for the development of advanced diagnostics and therapeutic systems and tools, since many diseases are induced by modified functionality of such entities due to changes in their structure or conformation. For example, protein misfolding and amyloid fibril formation is associated with Alzheimer disease⁵ and an increased size of saliva and urinary exosomes is correlated with the occurrence of oral⁶ and prostate cancers,⁷ respectively. On the other hand, the size of lipid nanoparticles and exosomes is also a critical parameter for their efficiency in drug delivery.^{8,9} At the same time, performing accurate size and shape determination of nanoscopic biological entities is challenging because they are “soft” and highly dynamic, and because their dimensions and conformation depend on interactions with other biological species or surfaces in their surroundings. To this end, various techniques have been used to quantify such systems, including transmission electron microscopy (TEM),¹⁰⁻¹² X-ray crystallography,^{13,14} neutron reflectometry,^{15,16} and nuclear magnetic resonance (NMR).^{17,18} However, TEM seldomly enables characterization of the dynamics of such processes and thus prohibits studies of conformational change in real-time.^{19,20} This is similar to X-ray crystallography due to its requirement of crystalline samples. In contrast, both neutron reflectometry and NMR permit the study of conformational dynamics, however, only with low throughput and high sample consumption.¹⁵⁻¹⁸

In this regard, optical sensing techniques, such as ellipsometry,²¹ silicon microring resonators (SMR),^{22,23} optical waveguide lightmode spectroscopy (OWLS)^{24,25} and surface plasmon resonance (SPR),²⁶⁻²⁸ are attractive tools since they provide sensitive, label-free and real-time detection with high throughput and

relatively simple instrumentation. Conceptually, these methods all measure the presence of, or a change in, a biomolecular layer formed on the sensor surface *via* changes in the interfacial refractive index. Due to a near linear correspondence between changes in this index and number of bound molecules, these methods are commonly used to measure the adsorbed molecular mass with high accuracy. Furthermore, by employing intricate modelling and multiparameter measurements, both the refractive index and thickness of the biomolecular layer can be determined using these methods. Specifically, with state-of-the-art instrumentation and careful calibration of the substrate and solutions, ellipsometry, SMR, and OWLS can be used to quantify dense biomolecular layers with thicknesses down to 2 nm,^{22,23,29,30} and using multi-mode optical excitation concepts, similar deconvolutions are possible in the case of SPR.^{22,23,25,31,32}

In this respect, the dual-mode SPR approach introduced by Rupert *et al.*³³ for quantification of nanoparticle size and structure is of particular relevance for our work. They utilized and extended a formalism derived from the characteristic response of an SPR sensor^{32,34} that relates the ratio of the wavelength-shift response of the two considered SPR modes to the size and RI of the studied systems.³³ However, due to the large extension of the evanescent field from the surface in SPR (100–400 nm), this method is fairly accurate in quantification of mass of nanoparticles on this or smaller length scale but not suitable for characterization of the shape of nanoparticles with sizes smaller than few tens of nanometers.

In contrast, localized surface plasmon resonance (LSPR)-based sensors hold promise for characterization of thinner/smaller adsorbates due to the significantly shorter field decay lengths,³⁵ and have been successfully employed to determine distances of few nanometers between, *e.g.*, two plasmonic antennas, an antenna and a mirror, and an antenna and a biological layer.^{36–39} Furthermore, they have been used to scrutinize changes of the shape of adsorbed biomolecules⁴⁰ and biological nanoparticles, such as lipid vesicles under various conditions,^{40–44} and have been employed to investigate the remodeling of a supported lipid bilayer with the formation of buds and tubules.⁴⁵ In such studies, the LSPR sensors can be viewed as a nanoplasmonic ruler that enables thickness measurements. To this end, in a very recent attempt to combine SPR and LSPR, Mataji-Kojouri *et al.* have developed a Fabry-Perot cavity array that supports these modes in the same structure, which enabled the determination of the thickness of a biomolecular layer in the range of 10-100 nm, with 4 nm resolution.³¹

To push the plasmonic nanoruler concept to the regime where accurate layer thickness determination becomes possible with sub-nanometer resolution, we introduce here a dual-band nanoplasmonic ruler comprising two mixed populations of plasmonic nanoantennas with distinctly different size that gives rise to two independent LSPR peaks in their extinction spectrum. Due to the short-range evanescent fields created by the resonating antennas, this approach enables real-time and accurate thickness and RI determination in the sub-10 nm layer thickness range. To corroborate this dual-band nanoplasmonic ruler concept theoretically, we first thoroughly assess the applicability of the formalism introduced by Rupert *et al.*³³ for SPR sensors to LSPR sensors using electrodynamic simulations based on the finite-difference

time-domain (FDTD) method, and use it to rationally design the ruler that we subsequently implement in practice. For that purpose, we employ a tailored version of hole-mask colloidal lithography and demonstrate the ability of the nanofabricated dual-band nanoplasmonic ruler to accurately measure and temporally resolve thickness change in different systems and settings: (i) atomic layer deposition of an Al₂O₃ film in air and (ii) adsorption of 35 nm lipid vesicles with subsequent spontaneous formation of a planar supported lipid bilayer (SLB) on silica in liquid, (iii) adsorption of 10 nm SiO₂ nanospheres onto an SLB, and (iv) quantification of the shape changes of adsorbed lipid vesicles during SLB formation, demonstrating sub-nanometer resolution up to thickness accumulation/change of 60 nm.

Results And Discussion

Theoretical Background

In conventional SPR, the response (or, more specifically, the shift in either wavelength or angle of the SPR minimum) associated with changes of the RI and/or thickness and shape of a nanosized analyte (referred to below as “layer”) in contact with the metal surface of the sensor can be analytically described as (see Eq. 6 in combination with Eq. 4 in Ref. 33)

$$R = S \left(n_{layer} - n_{bulk} \right) \frac{v_{cp}}{\delta} \phi$$

1
,

where S is the sensor sensitivity, n_{bulk} and n_{layer} are the bulk and layer RIs, respectively, v_{cp} is the molecular analyte volume per unit area (in fact, this is the average thickness of the analyte layer, *i.e.*, the thickness calculated with the close-packed arrangement of analyte atoms or molecules), ϕ (≤ 1 , or 1 provided the layer is thin and the field extinction is negligible) is a dimensionless factor taking the decay of the intensity of the evanescent field into account that is defined (Eq. 7 in Ref. 33) as normalized convolution of the analyte-mass distribution with the exponential attenuation function $\exp(-z/\delta)$, and δ is the corresponding decay length. This expression for R depends on the analyte optical properties *via* n_{layer} and geometry *via* ϕ , and accordingly their values cannot be inferred simultaneously from measurements at a single frequency. With two frequencies (associated below with subscripts 1 and 2), however, this is possible and it is convenient to use the ratio of the two readouts (Eq. 15 in Ref. 33),

$$\frac{R_1}{R_2} = \frac{S_1 \left(n_{layer1} - n_{bulk1} \right) \phi_1 \delta_2}{S_2 \left(n_{layer2} - n_{bulk2} \right) \phi_2 \delta_1}$$

2
,

In applications, the values of all the parameters (except φ_1 and φ_2) are either known or their ratio can be determined by performing measurements in the thin-layer limit (with $\varphi_1 = \varphi_2 = 1$). Then Eq. 2 can be applied to the layers with arbitrary fine structure and size, and these properties can be characterized *via* the ratio φ_1/φ_2 . We are interested below primarily in a uniform close-packed layer of thickness d_{layer} with $v_{cp} = d_{layer}$, and (Eq. 14 in Ref. 33)

$$\phi = [1 - \exp(-d_{layer}/\delta)] \frac{\delta}{d_{layer}}$$

3

.

In this case, Eqs. 1 and 2 can, respectively, be rewritten as

$$R = S(n_{layer} - n_{bulk})[1 - \exp(-d_{layer}/\delta)]$$

4

,

and

$$\frac{R_1}{R_2} = \frac{S_1(n_{layer1} - n_{bulk1})[1 - \exp(-d_{layer}/\delta_1)]}{S_2(n_{layer2} - n_{bulk2})[1 - \exp(-d_{layer}/\delta_2)]}$$

5

.

It is now of our interest here to investigate in which way this SPR formalism can be applied to an LSPR sensor. For this purpose, we first remind that in SPR, the decay of the evanescent field is exponential and the corresponding decay length, δ , is defined by the light frequency and optical constants of the media. In LSPR, in contrast, the evanescent field around sensing nanoantennas contains different terms (dipole, *etc.*), and the corresponding decay length is roughly proportional to and significantly smaller than the antenna size. In addition, one should operate by the permittivities rather than by RIs. At the simplest level this difference can be taken into account in the dipole approximation by just replacing the exponential attenuation function, $\exp(-z/\delta)$, in the calculation of φ by the power-law function, $\sim 1/(R_* + z)^6$, where R_* is the length scale (effective radius) characterizing plasmonic nanoantennas.⁴³ In the context of applications, the difference between these two approaches is often minor.⁴⁴ For this reason, we use here the conventional exponential approximation, or more specifically Eqs. 4 and 5, in the LSPR case in order to articulate the analogy between SPR and LSPR, as often done in the earlier literature since the first

applications of LSPR (see, *e.g.* Ref. 46). In particular, we identify S with the bulk refractive index sensitivity, $BRIS$ (to be distinguished from the local sensitivity of an LSPR sensor), and rewrite Eq. 5 as

$$\frac{\Delta\lambda_{peak1}}{\Delta\lambda_{peak2}} = \frac{BRIS_1 (n_{layer1} - n_{bulk1}) [1 - \exp(-d_{layer}/\delta_1)]}{BRIS_2 (n_{layer2} - n_{bulk2}) [1 - \exp(-d_{layer}/\delta_2)]}$$

6

where $\Delta\lambda_{peak\ i}$ ($i = 1$ or 2) are the analyte-induced LSPR peak position shifts of two sensing plasmonic nanoantennas. Since both resonances practically measure the same analyte layer in the same medium, and in our context the dependence of n_{layer} and n_{bulk} on the light frequency is negligible,⁴⁷ *i.e.*, $n_{layer\ 1} = n_{layer\ 2}$, and $n_{bulk\ 1} = n_{bulk\ 2}$, the expression can be further simplified to

$$\frac{\Delta\lambda_{peak1}}{\Delta\lambda_{peak2}} = \frac{BRIS_1 [1 - \exp(-d_{layer}/\delta_1)]}{BRIS_2 [1 - \exp(-d_{layer}/\delta_2)]}$$

7

This equation then contains only one unknown: the d_{layer} of the analyte layer, which can be conveniently derived given that $BRIS_i$ and δ_i have been previously determined in calibration experiments of the sensor. Eq. 7 forms the basis for our analysis below.

In the LSPR case, as already noted, Eqs. 6 and 7 correspond to the simplest phenomenological approximation containing one length scale, δ . This approximation is not exact even in the case of a uniform close-packed layer, because the evanescent field around sensing nanoantennas is inherently not exponential (it depends on their shape and is influenced by the support). Nevertheless, the usefulness of Eqs. 6 and 7 in the LSPR context has already been illustrated.^{46,48-50}

To explicitly clarify this aspect in our case, we employ finite-difference time-domain (FDTD) simulations to model LSPR sensors comprising Au nanodisks, with diameter spanning from 60 to 180 nm and thickness from 20 to 70 nm. The nanodisks are placed on a substrate with a RI of 1.5 and surrounded either by a medium with RIs ranging from 1.33 to 1.5 to emulate a BRIS experiment, or they are covered by a thin conformal layer of up to 20 nm thickness with RI up to 1.5 to emulate a molecular/thin layer sensing experiment. For the first scenario, the $BRIS$ is a linear function of the nanodisk dimensions and scales well across the simulated parameter range, as expected (Supplementary Figure 1). To showcase the key findings for the thin-layer sensing scenario, we use a nanodisk with diameter of 80 nm and thickness of 20 nm as example. However, instead of directly plotting the obtained peak shift $\Delta\lambda_{peak}$ *vs.* d_{layer} for different RIs of the layer, we modify the former into the following form:

$$\log \left[1 - \frac{\Delta \lambda_{peak}}{BRIS(n_{layer} - n_{bulk})} \right] = - \frac{d_{layer}}{\delta}$$

8

which is derived from Eq. 4 with appropriate parameters for an LSPR sensor (*i.e.*, $\Delta \lambda_{peak}$ and $BRIS$ replacing R and S , respectively). The fit of our FDTD calculations by using the left-hand part of Eq. 8 is close to linear, as predicted by Eq. 4 (Fig. 1a). Thus, Eqs. 4 and 7 indeed describe our system in an acceptable way. In addition, our calculations show that, as expected,⁵¹ (i) the dependence of δ on RIs is very weak and thus can be neglected (Fig. 1b), and (ii) δ is significantly shorter than the size (diameter) of the sensing nanoantenna and increases with increasing this size, because the decay of the evanescent field is determined primarily by the shape of the nanoantenna (in the dipole approximation,⁴³ one has $\delta \approx R^*/5$).

Nanoruler Design Considerations

Having confirmed the overall validity of our formalism for LSPR-based sensing, we apply it to design a dual-band nanoplasmonic sensor surface that we subsequently implement and explore experimentally. In this process, the first design consideration is to choose two plasmonic nanodisk types with spectrally non-overlapping LSPR modes, different decay lengths, and with sufficient sensitivities. To illustrate this concept explicitly, we simulated nanodisks with 80 and 160 nm diameter and identical thickness of 20 nm and placed a conformal dielectric thin layer with arbitrarily chosen thickness $d_{layer} = 9$ nm and RI $n_{layer} = 1.41$ on top of them to calculate the induced $\Delta \lambda_{peak}$ for both nanodisk sizes for this condition. While this is straightforward, if we subsequently want to reverse this process and back-calculate which combination of d_{layer} and n_{layer} that gave rise to the obtained $\Delta \lambda_{peak}$ values for each disk, it turns out to be essentially impossible since, as outlined above, a practically infinite combination of d_{layer} and n_{layer} will produce similar $\Delta \lambda_{peak}$. To illustrate this condition, we calculated all of these potential matches (d_{layer} from 0–20 nm and n_{layer} 1.35–1.5) for the two disks independently (Fig. 1c-d). Specifically, we plot the values of

$\log_{10} \left| \Delta \lambda_{peak} \frac{d_{layer}}{n_{layer}} - \Delta \lambda_{peak} \frac{9}{1.41} \right|$, in that the minima give the combination of d_{layer} and n_{layer} that results in similar $\Delta \lambda_{peak} \frac{9}{1.41}$. While separately the individual response of each of the two nanodisks is not unique with respect to d_{layer} and n_{layer} , the sum of these two plots yields a single point at which the two curves' minima intersect, which corresponds to the initially chosen values of $d_{layer} = 9$ nm and $n_{layer} = 1.41$, respectively (Fig. 1e). Mathematically, such a distinct intersection point can only be defined if the two disks have distinctly different sensitivities and decay lengths since the particular dependencies otherwise partially overlap rather than intersect each other. This, in turn, would result in a large uncertainty of the unique combination of layer thickness and RI that is compatible with the LSPR

response of both disk types. Hence, to realize a dual-band nanoplasmonic ruler, one has to employ two types of plasmonic nanoantennas with not only spectrally well-separated peaks but also with distinctly different sensitivities and field decay lengths.

Nanoruler Fabrication and Characterization

Conceptually, a nanoplasmonic ruler that can disentangle thickness and refractive index variations as outlined above can be accomplished by executing identical measurements on two separate plasmonic surfaces that feature spectrally separated resonance peaks. However, while such measurements are sufficient if one is interested in steady state conditions, they cannot temporally resolve the investigated processes, and therefore preclude analysis of, *e.g.*, kinetics, since it is almost impossible to have exactly identical conditions in separate experiments on two different surfaces. Therefore, we develop a nanoplasmonic ruler surface where two different nanoantenna types with distinctly different size and thus plasmon resonance wavelength are mixed within the same array and thus on the same surface. In this way, only one experiment is required to quantify thickness, refractive index and adsorbate shape, as well as temporal variations in the properties during dynamic processes.

To implement a dual-band nanoplasmonic ruler in line with this design principle, while simultaneously being compatible with the visible to near-infrared (NIR) wavelength range (400–1100 nm) most commonly used in the field,⁵² we identify two Ag nanodisk populations with 80 nm and 210 nm diameter, and similar height of 20 nm as the best-suited nanoantennas for our purpose.^{49,53} Specifically, due to Ag's narrow LSPR modes and interband absorption threshold of ~ 325 nm, a distinct spectral separation of the LSPR peaks can be obtained.

To implement these properties on a single surface, we employed a modified version of the hole-mask colloidal lithography (HCL)⁵⁴ method, using a polystyrene (PS) colloidal suspension for the self-assembly step, in which PS beads of two distinctly different sizes (here 74 and 210 nm nominal diameter) were mixed to create a HCL-mask with uniformly distributed holes of two different diameters defined by the beads (see Methods for details). Using this approach, we were able to produce mixed arrays of two nanodisk types with dissimilar sizes on a substrate in a single HCL fabrication cycle (Fig. 2a). Varying the relative concentration of the two types of beads in the mixed suspension offers a means to control the relative abundance of the two nanodisk sizes in the mixed array on the surface and thus the relative intensity of the respective LSPR peak, where the aim was to achieve roughly equal intensities (Supplementary Figure 2). To this end, mixing 0.02 *wt.*% of 74 nm PS beads and 0.1 *wt.*% of 210 nm PS beads in water results in randomly mixed nanodisks arrays whose extinction spectra exhibit two distinguishable LSPR peaks of similar intensity and with large spectral separation (Fig. 2b-d and also see Supplementary Figure 3 for the nanodisk size distribution). Finally, to introduce both long-lasting structural integrity and protection from harsh chemical and temperature conditions,^{49,55–57} as well as to provide a uniform chemical surface, we applied a thin conformal Si₃N₄ coating to the sensor surface (Fig. 2a). If needed, other coating materials can be utilized (*e.g.* SiO₂, TiO₂) to alter the interaction of the adsorbed films/biomolecules with the support.

With the sensor surface at hand, we next experimentally quantify the two key sensitivity descriptors of the two types of nanodisks in the array, namely their *BRIS* and field decay lengths δ . The *BRIS* is derived by correlating the shifts of the two LSPR peaks, $\Delta\lambda_{\text{peak}}$, to the RI of the medium the sensor is exposed to (Fig. 3a, see Supplementary Figure 4 for raw data). It is clear that the two nanodisk populations in the mixed array respond independently and exhibit different *BRIS*, *i.e.*, $BRIS_{\text{small}} = 51 \text{ nm/RIU}$ and $BRIS_{\text{large}} = 184 \text{ nm/RIU}$. These sensitivities are consistent with previous experimental and theoretical works demonstrating a positive correlation between a plasmonic particle size and *BRIS*.^{58,59}

To determine the field decay lengths of the two types of nanodisks in the mixed array, we applied the established method of subsequent atomic layer deposition of thin Al_2O_3 layers and fitting the resulting $\Delta\lambda_{\text{peak}}$ induced by the thickness accumulation of each layer to the local sensitivity of a plasmonic nanoantenna expressed in Eq. 4.^{34,48,49,60} As depicted in Fig. 3b, deposition of conformal Al_2O_3 thin layers up to 55 nm gives rise to increasing and eventually saturating $\Delta\lambda_{\text{peak}}$ for both small and large nanodisks. To this end, the small nanodisks reach $\Delta\lambda_{\text{peak}}$ saturation earlier, around a layer thickness of 40 nm, implying insensitivity to thickness change beyond this value. The large nanodisks on the other hand still exhibit a discernible $\Delta\lambda_{\text{peak}}$ even beyond a layer thickness of 55 nm due to their anticipated longer field decay length.^{49,51} To explicitly extract the decay length from our data, we fit the $\Delta\lambda_{\text{peak}}$ response to Eq. 4 and find $\delta_{\text{small}} = 14 \text{ nm}$ and $\delta_{\text{large}} = 28 \text{ nm}$. Notably, these values compare well to those of the Au nanodisks simulated above (*cf.* Fig. 1b).

After this analysis we have all the necessary input to construct the nanoruler conversion correlation given by Eq. 7 for our nanofabricated sensor (Fig. 3c). The obtained conversion plot provides a direct translation between the $\Delta\lambda_{\text{peak}}$ ratio between the large and small nanodisks obtained from a measurement and the corresponding thickness of an arbitrary layer deposited on the sensor. This conversion plot is strictly valid only for experiments conducted in air/gaseous environment. In other words, if the sensor surface is used for a measurement in other media, *e.g.* water, a new conversion plot needs to be constructed based on sensitivity parameters (in particular the decay lengths) determined in this medium. However, as we explicitly show below, by using a system with well-known thickness and RI in liquid medium, we can simplify the steps for finding the decay lengths of the nanodisks. Furthermore, now with the two sensitivity descriptors of the nanodisks known, modification of Eq. 4 also enables the nanoruler to determine the RI of the deposited layer, *i.e.*,

$$n_{\text{layer}} = \frac{\Delta\lambda_{\text{peak}i}}{BRIS_i \left[1 - \exp\left(-d_{\text{layer}}/\delta_i\right) \right]} + n_{\text{bulk}}$$

8

Finally, plotting the first derivative of the $\Delta\lambda_{\text{peak}}$ ratio with respect to the layer thickness allows us to also assess the sensitivity of such nanorulers in terms of the absolute $\Delta\lambda_{\text{peak}}$ ratio change per 1 nm change of

the layer thickness. As shown in Fig. 4, our system exhibits a corresponding sensitivity of $\sim 0.03 \Delta\lambda_{\text{peak}}$ ratio change for a layer thickness up to ~ 20 nm, which then gradually decreases to about one third of this value at a layer thickness of 60 nm. As a key point here, we highlight that the range within which the nanoruler exhibits the highest sensitivity towards a thickness change coincides well with the near field decay length of the plasmonic nanodisks, which is on the order of 20 nm. This is obvious when we compare the sensitivity of our nanorulers with others employing LSPR-SPR modes³¹ and dual SPR modes,³³ whose sensitivities are at least half, due to the much longer decay lengths, which are on the order of few hundred nanometers in the SPR case. As the key conclusion, this comparison thus highlights that our LSPR-based dual-band nanoruler is most suitable for measurements of layers in the few tens of nanometer thickness range.

Thickness and Refractive Index Determination of Single-Layer Accumulation in Air

With the overall concept and sensor surface established, we now apply it to measure the thickness of a single layer accumulated on the ruler surface. To do this, we can again resort to Al_2O_3 layer deposition, as used above for determining the decay lengths in air (Fig. 5a). Starting from the independent $\Delta\lambda_{\text{peak}}$ determined for both small and large nanodisks upon deposition of subsequent Al_2O_3 layers (*cf.* Fig. 3b), we can construct their $\Delta\lambda_{\text{peak}}$ ratio (Fig. 5b) and, for each of the $\Delta\lambda_{\text{peak}}$ ratios obtained after addition of a new Al_2O_3 layer, calculate a corresponding Al_2O_3 layer thickness by using the conversion (Fig. 3c). Comparing the layer thicknesses obtained in this way by the nanoruler with values obtained by ellipsometry for identical Al_2O_3 layers, reveals an excellent agreement for the whole measured range from 2 to 55 nm (Fig. 5c). Particularly noteworthy is that the nanoruler is able to distinctly resolve the layer thickness in the sub-10 nm thicknesses regime with a maximum absolute thickness difference between the nanoruler and ellipsometry of only 0.6 nm – a significant improvement of accuracy compared to other nanorulers.³¹ Furthermore, as discussed above, the nanoruler is also capable of measuring the RI of the Al_2O_3 layer, which again is in excellent agreement with the value obtained by ellipsometry (Fig. 5d).

Thickness and Refractive Index Determination of Biomolecular and SiO_2 Nanosphere Layer Accumulation in Liquid Medium

As a second demonstration of the dual-band LSPR nanoruler, we use it to characterize the multistep deposition of a supported lipid bilayer (SLB), followed by small SiO_2 nanosphere adsorption (Fig. 6a). Specifically, we first expose the nanoruler sensor to a lipid vesicle suspension (1-palmitoyl-2-oleyl-sn-glycero-3-phosphocholine, POPC) in BIS TRIS buffer, while continuously tracking the $\Delta\lambda_{\text{peak}}$ of the two disk populations. Once saturation of the $\Delta\lambda_{\text{peak}}$ is reached, which together with the observed characteristic “kink” in the plasmonic sensor signal (at *ca.* min 10) imply that the POPC vesicles have

ruptured and formed an SLB on the nanoruler,⁶¹ a rinsing step with pure buffer is applied to remove excess vesicles. Subsequently, we expose the nanoruler to a suspension of 7 nm SiO₂ nanospheres, which physisorb onto the SLB. At the end, once $\Delta\lambda_{\text{peak}}$ saturation again has been reached, a pure buffer rinse is applied to remove unbound spheres, leaving a monolayer of SiO₂ nanospheres on the SLB. It is noteworthy that in these experiments, the SLB represents a nearly perfectly uniform layer, and accordingly can be characterized by using the nanoruler under consideration. In contrast, SiO₂ nanospheres represent a heterogeneous layer, and it is expected to be characterized by the nanoruler with the simplest expression (Eqs. 6 and 7) only provided the nanosphere size is smaller than or comparable to δ that corresponds to the smaller sensing nanodisks. The size of the SiO₂ nanospheres chosen for our experiment satisfies this condition.

To start the quantitative analysis and discussion of this experiment, we plot the $\Delta\lambda_{\text{peak}}$ signals of the small and large nanodisks as a function of time, along which the specific steps described above (Fig. 6b). Comparing the $\Delta\lambda_{\text{peak}}$ signals after the first rinse with the starting point of the experiment reveals an irreversible $\Delta\lambda_{\text{peak}}$ of 2.2 nm for the small disk peak and of 4.3 nm for the large disk peak, in good agreement with results from plasmonic sensors with single-type nanodisks,^{39,42,62} thereby confirming the SLB formation. Looking then at the SiO₂ nanosphere adsorption phase, a sudden $\Delta\lambda_{\text{peak}}$ and distinct increase and saturation of $\Delta\lambda_{\text{peak}}$ for both nanodisk sizes occurs, corroborating the adsorption of nanospheres on the SLB. At this point, we also note that we observe different trends during the rinsing step following the exposure to POPC vesicles and SiO₂ nanospheres in that in the former case both $\Delta\lambda_{\text{peak}}$ signals decrease, while they increase in the latter case. Intuitively, one could assign such peak change to a decrease and increase of the layer thickness, respectively, which, however, may not be the case, as we discuss below.

As the next step, we plot the $\Delta\lambda_{\text{peak}}$ ratios for the entire POPC and SiO₂ nanosphere deposition, which reproduces the key features corresponding to the different steps of the process (Fig. 6c). To this end, we specifically highlight the distinct break in overall trend at the position of the “kink”, where vesicle rupture is initiated. To now be able to derive the ratio-to-thickness conversion plot, the field decay lengths of the small and large nanodisks in water are required. To obtain them, we can utilize the formed SLB, since its thickness and RI are well-known and have been quantified in multiple works to be ~5 nm and ~1.48, respectively.^{63,64} Using these numbers, we can therefore back-calculate the decay lengths of the two disks for our system in water through modification of Eq. 4 to

$$\delta_i = - \frac{d_{\text{layer}}}{\log \left[1 - \frac{\Delta\lambda_{\text{peak}i}}{\text{BRIS}_i (n_{\text{layer}} - n_{\text{bulk}})} \right]}$$

and by assigning the thickness and RI of the SLB to the value of the $\Delta\lambda_{\text{peak}}$ obtained during the SLB formation in our experiment, *i.e.*, 4.3 nm and 2.2 nm for small and large nanodisks, respectively (Fig. 6b). This procedure yields a decay length of 14 nm and 29 nm for the small and large nanodisks, respectively, which are slightly different than those in air derived above, as expected.⁴⁹ With this input, we construct the conversion plot for water environment (Supplementary Figure 6). This method of determining the decay length by using a well-known system like an SLB is (much) less tedious than using subsequent deposition of Al_2O_3 layers, as we have done first. Furthermore, and most importantly, it has the additional advantage that an SLB can be efficiently removed by mild detergents after such a calibration experiment, making the nanoruler available for subsequent experiments on a system with unknown thickness and/or RI (Supplementary Figure 5).

As the final step, we use the conversion plot to extract the thickness evolution of the layers on the surface of the nanoruler during the course of our experiment (Fig. 6d). Focusing again first on the SLB formation phase, we find that at the end of the rinsing step the SLB exhibits a thickness of 5 nm, which is 1 nm less than the one prior to rinsing but after completed SLB formation. This can be attributed to the removal of excess lipids and lipid vesicles associated with the SLB during the rinsing and gives a first indication of the detection limit of our nanoruler. At the same time, we also highlight that the 5 nm thickness value *per se* is neither surprising nor an indication of the performance of the nanoruler since it was used for the decay length determination above. A much more curious and significant result is observed in the phase before the SLB formation is completed, *i.e.*, during the vesicle adsorption and rupture. Specifically, the data reveal an initial thickness buildup up to around 15 nm, after which a sudden and rapid thickness decrease occurs. Interestingly, the transition point accurately coincides with the “kink” observed in the $\Delta\lambda_{\text{peak}}$ data, which commonly is associated with the onset of vesicle rupture when they have reached their critical surface concentration (*cf.* Fig. 6b). Hence, this experiment confirms the mechanism proposed to be responsible for the “kink” in a plasmonic sensor signal.⁶¹ Furthermore, as we elaborate later below, by establishing a correlation between the $\Delta\lambda_{\text{peak}}$ ratio of our nanoruler and the geometry of adsorbed vesicles, we can measure the degree of deformation of vesicles at the critical coverage before rupture.

Focusing here first on the SiO_2 nanosphere adsorption, we see a distinct thickness increase from 5 nm to 16 nm, followed by a slightly reduced thickness of 14 nm after rinsing, which we attribute to removal of loosely bound nanospheres. Since this is a cumulative thickness that includes the thickness of the SLB, we can deduce that the formed SiO_2 nanosphere monolayer comprises particles with average diameter of 9 nm. Remarkably, independent size assessment of the nanospheres using transmission electron microscopy (TEM) reveals an average particle diameter of 11 ± 2 nm, which is in good agreement with the number derived with the nanoruler (inset in Fig. 6d). We note that the diameter obtained here is slightly larger than the nominal one (*i.e.*, 7 nm) and speculate that this difference arises as a consequence of the method used to determine it. To this end, the nominal diameter of the SiO_2 nanoparticles was derived *via* conversion of the specific surface area (SSA) obtained using the Brunauer–Emmett–Teller (BET) method.⁶⁵ BET, however, only permits characterization of dried samples that are prone to agglomeration and consequently results in lower apparent SSA and thus smaller inferred particle diameter.⁶⁶

Last, we return to the observation that $\Delta\lambda_{\text{peak}}$ was found to increase during the rinsing after SiO_2 nanosphere adsorption (*cf.* Fig. 6b), which we tentatively had ascribed to a thickness increase of the formed layer. However, as the thickness analysis reveals, this is not the case and we actually observe a slight apparent decrease of the SiO_2 nanosphere layer thickness (Fig. 6d). In this case, it is accompanied by an increase in the RI of the SiO_2 monolayer (Fig. 6e), which presumably forms a denser layer during the rinsing. We tentatively attribute this to partial SLB formation on the SiO_2 nanospheres with a lower RI than that of lipids, and highlight that this type of information cannot be deduced with certainty using a conventional single-peak plasmonic sensor.

To determine the resolution of the nanoruler developed here, we assess its noise both in terms of $\Delta\lambda_{\text{peak}}$ ratio and the deduced layer thickness at two different cases. Fig. 6f-g shows the acquired $\Delta\lambda_{\text{peak}}$ ratio at complete formation of SLB and monolayer of SiO_2 nanospheres, respectively. Clearly, at two cases the $\Delta\lambda_{\text{peak}}$ ratio noise, σ_r , is similar, that is, 0.004. This number is extremely low and referring back to Fig. 4, it is lower than the nanoruler sensitivity and therefore, considering a detection limit of $3\sigma_r$, it confirms the nanorulers' ability to resolve sub-1 nm thickness changes up to an accumulated thickness of 60 nm. Indeed, this claim holds true also when we infer the resulting thickness determination noise, σ_b , on the scale of 0.13 nm (Fig. 6h-i). Therefore, with the limit of detection defined as $3\sigma_b$, our nanoruler should in principle be able to distinguish thickness differences of ~ 0.5 nm for layers in the few tens of nanometer thickness range. This is among the highest resolution achieved for a *functional* optical nanoruler.^{22,31}

Determination of the Degree of Vesicle Deformation prior to Rupture

As the last analysis related to the capability of our nanoruler, we investigated the dynamic changes of the response upon SLB formation in an attempt to determine the thus far elusive degree of deformation of adsorbed vesicles at the onset of SLB formation. As illustrated in Fig. 6a, upon adsorption, vesicles are expected to conform to squished, truncated spheres, whose deformation at a critical elongated contact to the support triggers rupture and fusion with nearby vesicles and thus defines the onset of SLB formation. Identifying the vesicle deformation required for this onset of rupture and fusion at the critical vesicle coverage constitutes one of the most central and long-standing questions in this field.^{40,44,67-69} To this end, the related indirect data were long indicative that the deformation required is sizable but not dramatic (see *e.g.* Ref. 70).

To set the stage for such determination using our nanoruler, it is crucial to recall that Eq. 4 operates at the level of a uniform film. In the case of adsorbed deformed vesicles, however, the film should be represented as a convolution of two thicknesses, that is a planar region with a thickness equal to that of the SLB with a contact length defined by radius a , and an additional thickness comparable to the deformed vesicle radius ρ (Fig. 7a). In other words, Eq. 4 is obviously insufficient or not fully sufficient for such case. However, as already noticed, Eq. 4 can be extended as earlier proposed for dual-band SPR³³ or

single-band LSPR.^{40,44,45} Following this line, we illustrate how the former formalism can be applied to our dual-band LSPR ruler.

To give an accurate contribution of the deformed vesicle shape to the optical signal in our sensor, we replace Eq. 3 by (see Eq. S1 in Ref. 33, and note that there is a misprint that we correct here)

$$\phi = \left[a^2 + 2\rho\delta(1 - \exp\{-[\rho + (\rho^2 - a^2)^{\frac{1}{2}}]/\delta\}) \right] / 4r^2$$

10

where ρ is geometrically connected to a through

$$\rho = (4r - a^2/r) / (16 - 8a^2/r^2)^{1/2}$$

11

with r being the initial radius of the vesicles (Fig. 7a). Using Eqs. 1 and 10, and again converting the relevant parameters to the corresponding LSPR analogues, we express the $\Delta\lambda_{\text{peak}}$ ratio of our nanoruler to the deformation degree of vesicles expressed *via* the contact length (Fig. 7b)

$$\frac{\Delta\lambda_{\text{peak1}}}{\Delta\lambda_{\text{peak2}}} = \frac{BRIS_{\text{large}}}{BRIS_{\text{small}}} \frac{a^2/\delta_{\text{large}} + 2\rho(1 - \exp\{-[\rho + (\rho^2 - a^2)^{\frac{1}{2}}]/\delta_{\text{large}}\})}{a^2/\delta_{\text{small}} + 2\rho(1 - \exp\{-[\rho + (\rho^2 - a^2)^{\frac{1}{2}}]/\delta_{\text{small}}\})}$$

12

To finally identify the critical contact length of the deformed vesicles prior to rupture, we go back to the data presented in Fig. 6c. As previously discussed, the onset of the vesicle rupture is marked by the sudden drop in the $\Delta\lambda_{\text{peak}}$ ratio, where the ratio reaches the value of 2.18. By using the conversion plot presented in Fig. 7b, the critical contact length is found to be 35.4 nm (with the corresponding height of 24.4 nm). This result is compelling as it suggests that the vesicles will only rupture once their contact length to the support is as wide as its original diameter (Fig. 7c). In a more general context, our quantitative result is comparable with those suggested for larger vesicles (~100 nm) on TiO₂ by using LSPR⁴⁰ and for vesicles (~170 and ~100 nm) linked to the support *via* biotin-streptavidin complexes studied by using SPR³³ and LSPR,⁴⁰ respectively.

Conclusions

In summary, we have developed a dual-band nanoplasmonic ruler, capable of determining in real-time the change in thickness and refractive index of arbitrary (multi)layers, and the shape of nanoparticles deposited on top of it, with sub-nanometer resolution. We achieved such functionality by theoretically and experimentally devising a plasmonic sensor surface comprising two differently-sized nanoantennas that independently probe adlayers, and conjointly disentangle the sensor readout contribution from the adlayers' change in thickness, refractive index and shape. Proof-of-principle measurements in air and liquid environments corroborate the accuracy of our ruler, which is able to resolve sub-nanometer thickness changes for systems with up to 60 nm total thickness. This performance stands out among other optical nanorulers and, with its label-free, real-time and high throughput traits, advertises it as a promising tool to address important questions related to size and conformation in nanoscopic biological entities and, potentially, in materials science. To this end, we have here applied it to provide the first direct measurement of the degree of deformation of lipid vesicles at the critical coverage just prior to rupture and SLB formation on SiO₂. Looking forward, translating the dual-antenna concept into a flat surface type sensor^{62,71} would benefit the ruler in the form of more homogeneous evanescent fields and lack of surface corrugation. Furthermore, even higher thickness change resolution can likely be achieved by appropriate data post-processing.⁷²

Methods

Sensor Fabrication

Hole-mask colloidal lithography⁵⁴ (HCL) was used to fabricate the sensors. The details of the process undertaken (*e.g.*, materials, fabrication steps and equipment) are described elsewhere.^{49,73} Specific to the current work, a mixture of polystyrene beads with nominal diameter of 74 nm and 210 nm (Interfacial Dynamics Corporation) was diluted in Milli-Q water. To ensure thorough mixing, the suspension was sonicated for at least 30 min. Specific to the HCL process, the tape-stripping step was done twice to ensure all (differently sized) polystyrene beads were completely removed. As a final step, the thin conformal Si₃N₄ coating layer was deposited in an STS PE-CVD system.

Chemicals and Materials

Anhydrous chloroform (C 99%), glycerol (C 99%), HCl (1 M), NaCl (C 99%), bis(2-hydroxyethyl)amino-tris-(hydroxymethyl)-methane (Bis-Tris, C 98%), 1-palmitoyl-2-oleoyl-glycero-3-phosphocholine (POPC) were purchased from Merck Sigma-Aldrich (Darmstadt, Germany). Water used was of Milli-Q purity (resistivity 18.2 Ω·cm, Merck Millipore, Molsheim, France). All buffers had pH = 7.0, 150 mM NaCl, and 10 mM Bis-Tris. The pH was determined using a Mettler-Toledo (Ohio,US) pH meter. Buffers were sterilized either by autoclaving at 120 °C for 20 min or by sterile filtration using 0.22 μm Stericup-GV Sterile Vacuum filters (Millipore, France). The colloidal amorphous SiO₂ nanospheres (Bindizil 30/360, first number denotes weight concentration, *wt.*%, and second surface area per weight, m²/g) were obtained from AkzoNobel

PPC AB (Gothenburg, Sweden). The nominal diameter (7 nm) was calculated as the equivalent spherical diameter based on SSA measurements.

POPC Vesicles Preparation

POPC was dissolved in chloroform and dried in a 50 mL round flask under vacuum at 60 °C using a rotavap setup. The dried lipids were left under vacuum overnight to get rid of any residual chloroform. The dried POPC was then rehydrated in H₂O-based buffer to a concentration of 1 mg mL⁻¹, followed by a very brief bath sonication to dissolve any small traces of lipids on the walls of the flask. The POPC solution underwent five freeze/thawing cycles. After which, the solution was tip-sonicated for 30 min with intervals of 2 s pulse followed by 3 s pause to avoid overheating of the sample. Afterwards the sample was centrifuged a 20000×g for 30 min to get rid of any residuals from the tip of the sonicator. The POPC solution was finally extruded 11 times through 30 nm polycarbonate membranes (Whatman, UK) using a mini-extruder (Avanti, USA). The resulting vesicles are typical 35 nm in diameter as determined using dynamic light scattering (DLS).

Flow measurements: A commercial titanium flow cell (XNano, Insplorion AB) was used. All flow experiments were conducted under a constant flow of 100 µL/min, as regulated by a peristaltic pump (Ismatec). The sensor was illuminated using a fiber-coupled halogen lamp (AvaLight-Hal, Avantes) while the extinction spectra were continuously recorded by a fiber-coupled fixed grating spectrometer (AvaSpec-HS-TEC, Avantes). Bulk refractive index sensitivity was derived by exposing the nanoruler surface to mixtures of Milli-Q water (Millipore) and ethylene glycol (Sigma Aldrich) at mixing ratios 100:0, 80:20, 60:40, 40:60 and 20:80 wt.%. The λ_{peak} response was derived by fitting a Lorentzian to the spectra.⁷² Prior to flow experiments, the sensor was exposed to UV ozone for 3 min.

Decay length determination using Al₂O₃ layer-by-layer deposition: To determine the decay lengths of the two nanodisk populations on the nanoruler surface, subsequent thin Al₂O₃ layers were grown by atomic layer deposition (ALD, Oxford FlexAl). Intermittently, the layer thickness (deposited on an analogue silicon chip simultaneously) was evaluated by ellipsometry (J.A. Woollam M2000) and the extinction spectra were recorded using a Cary 5000 spectrophotometer. Great care was taken to ensure that the spectra were always acquired from the same spot on the sample.

FDTD simulations

The electromagnetic simulations were carried out using the finite-difference time-domain method as implemented in the software FDTD Solutions. The Au nanodisks, whose permittivity was taken from measurements by Johnson and Christy,⁷⁴ were modelled as flat cylinders with both top and bottom edges being rounded. The radius and height of the nanodisks spanned the range from 20 to 90 nm and from 20 to 70 nm, respectively. The nanodisks were placed on a substrate with a RI of 1.5. When modelling bulk sensitivity, the superstrate's RI was varied from 1.33 to 1.5. For local sensing of a conformal layer, the superstrate was taken always as water ($n = 1.33$). The thickness of the conformal layer, which covered

both the nanodisk and the substrate, ranged from 1 to 20 nm and its RI spanned from 1.37 up to 1.5. The simulation volume around the LSPR sensor had a mesh step of 0.5 nm. Perfectly matched layer absorbing boundary conditions were used to terminate the simulation volume and a linearly polarized plane wave excitation source was introduced *via* a total-field/scattered-field scheme.

Declarations

Acknowledgements

This research has received funding from the Knut and Alice Wallenberg Foundation project 2016.0210, from the Swedish Foundation for Strategic Research Framework project RMA15-0052, and the Polish National Science Center project 2017/25/B/ST3/00744. F.A.A.N. acknowledges support from the European Union's Horizon 2020 research and innovation programme under the Marie Skłodowska-Curie Grant Agreement No. 101028262. Part of this work was carried out at the MC2 cleanroom facility and at the Chalmers Materials Analysis Laboratory, and under the umbrella of the Chalmers Excellence Initiative Nano.

Author Contributions

F.A.A.N., T.J.A and C.L. conceived the idea. F.A.A.N. fabricated, characterized, and performed measurements on the nanorulers, analyzed the data and wrote the manuscript. D.S. and T.J.A. executed the FDTD simulation. A.A. and F.H. suggested and prepared the vesicles and buffer solution. P.O. and I.D. participated in fabrication and measurements of the nanorulers. S.N. carried out the TEM measurements. V.P.H. and F.H. provided the analytical expression of the nanoruler. C.L. coordinated the project. All authors critically commented on and revised the manuscript.

Corresponding Authors

*(FAAN): ferryanggoroardynugroho@yahoo.com (TJA): tomasz.antosiewicz@fuw.edu.pl (CL): clangham@chalmers.se

Competing Financial Interest

CL is co-founder of a company that markets nanoplasmonic sensors. The rest of the authors declare no competing interest.

Additional Information

Supplementary Information is available in the online version of the paper. Reprints and permissions information is available online at www.nature.com/reprints.

References

1. Ellison, C. J. & Torkelson, J. M. The distribution of glass-transition temperatures in nanoscopically confined glass formers. *Nature Materials* **2**, 695–700 (2003).
2. Scholl, J. A., Koh, A. L. & Dionne, J. A. Quantum plasmon resonances of individual metallic nanoparticles. *Nature* **483**, 421–427 (2012).
3. Bell, A. T. The impact of nanoscience on heterogeneous catalysis. *Science* **299**, 1688–1691 (2003).
4. Jiang, W., Kim, B. Y. S., Rutka, J. T. & Chan, W. C. W. Nanoparticle-mediated cellular response is size-dependent. *Nature Nanotechnology* **3**, 145–150 (2008).
5. Selkoe, D. J. Cell biology of protein misfolding: The examples of Alzheimer's and Parkinson's diseases. *Nature Cell Biology* **6**, 1054–1061 (2004).
6. Sharma, S., Gillespie, B. M., Palanisamy, V. & Gimzewski, J. K. Quantitative nanostructural and single-molecule force spectroscopy biomolecular analysis of human-saliva-derived exosomes. *Langmuir* **27**, 14394–14400 (2011).
7. Yang, J. S., Lee, J. C., Byeon, S. K., Rha, K. H. & Moon, M. H. Size Dependent Lipidomic Analysis of Urinary Exosomes from Patients with Prostate Cancer by Flow Field-Flow Fractionation and Nanoflow Liquid Chromatography-Tandem Mass Spectrometry. *Analytical Chemistry* **89**, 2488–2496 (2017).
8. Caponnetto, F. *et al.* Size-dependent cellular uptake of exosomes. *Nanomedicine: Nanotechnology, Biology, and Medicine* **13**, 1011–1020 (2017).
9. Arteta, M. Y. *et al.* Successful reprogramming of cellular protein production through mRNA delivered by functionalized lipid nanoparticles. *Proceedings of the National Academy of Sciences* **115**, E3351–E3360 (2018).
10. Schuller, J. M., Falk, S., Fromm, L., Hurt, E. & Conti, E. Structure of the nuclear exosome captured on a maturing preribosome. *Science* **360**, 219–222 (2018).
11. Jackson, C. L. *et al.* Visualization of dendrimer molecules by transmission electron microscopy (TEM): Staining methods and cryo-TEM of vitrified solutions. *Macromolecules* **31**, 6259–6265 (1998).
12. Wu, H., Friedrich, H., Patterson, J. P., Sommerdijk, N. A. J. M. & Jonge, N. Liquid-Phase Electron Microscopy for Soft Matter Science and Biology. *Advanced Materials* **32**, 2001582 (2020).
13. Ilari, A. & Savino, C. Protein structure determination by X-ray crystallography. *Methods in Molecular Biology* **452**, 63–87 (2008).
14. Powell, D. R. Review of X-Ray Crystallography. *Journal of Chemical Education* **93**, 591–592 (2016).
15. Penfold, J. & Thomas, R. K. The application of the specular reflection of neutrons to the study of surfaces and interfaces. *Journal of Physics: Condensed Matter* **2**, 1369–1412 (1990).
16. Fragneto-Cusani, G. Neutron reflectivity at the solid/liquid interface: Examples of applications in biophysics. *Journal of Physics Condensed Matter* **13**, 4973–4989 (2001).
17. Wishart, D. S., Sykes, B. D. & Richards, F. M. Relationship between nuclear magnetic resonance chemical shift and protein secondary structure. *Journal of Molecular Biology* **222**, 311–333 (1991).

18. Kaplan, M., Pinto, C., Houben, K. & Baldus, M. Nuclear magnetic resonance (NMR) applied to membrane–protein complexes. *Quarterly Reviews of Biophysics* **49**, e15 (2016).
19. Wang, C., Qiao, Q., Shokuhfar, T. & Klie, R. F. High-resolution electron microscopy and spectroscopy of ferritin in biocompatible graphene liquid cells and graphene sandwiches. *Advanced Materials* **26**, 3410–3414 (2014).
20. Park, J. *et al.* Direct Observation of Wet Biological Samples by Graphene Liquid Cell Transmission Electron Microscopy. *Nano Letters* **15**, 4737–4744 (2015).
21. Mora, M. F., Wehmeyer, J. L., Synowicki, R. & Garcia, C. D. Investigating Protein Adsorption via Spectroscopic Ellipsometry. in *Biological Interactions on Materials Surfaces* 19–41 (Springer US, 2009). doi:10.1007/978-0-387-98161-1_2.
22. Juan-Colás, J., Krauss, T. F. & Johnson, S. D. Real-Time Analysis of Molecular Conformation Using Silicon Electrophotonic Biosensors. *ACS Photonics* **4**, 2320–2326 (2017).
23. Hoste, J.-W., Werquin, S., Claes, T. & Bienstman, P. Conformational analysis of proteins with a dual polarisation silicon microring. *Optics Express* **22**, 2807 (2014).
24. J, V. *et al.* Optical grating coupler biosensors. *Biomaterials* **23**, 3699–3710 (2002).
25. Cross, G. H. *et al.* A new quantitative optical biosensor for protein characterisation. *Biosensors and Bioelectronics* **19**, 383–390 (2003).
26. Anker, J. N. *et al.* Biosensing with plasmonic nanosensors. *Nature Materials* **7**, 442–453 (2008).
27. Jackman, J. A., Rahim Ferhan, A. & Cho, N.-J. Nanoplasmonic sensors for biointerfacial science. *Chem. Soc. Rev.* **46**, 3615–3660 (2017).
28. Abdulhalim, I., Zourob, M. & Lakhtakia, A. Surface plasmon resonance for biosensing: A mini-review. *Electromagnetics* **28**, 214–242 (2008).
29. Mashaghi, A., Swann, M., Popplewell, J., Textor, M. & Reimhult, E. Optical Anisotropy of Supported Lipid Structures Probed by Waveguide Spectroscopy and Its Application to Study of Supported Lipid Bilayer Formation Kinetics. *Analytical Chemistry* **80**, 3666–3676 (2008).
30. Richter, R. P., Rodenhausen, K. B., Eisele, N. B. & Schubert, M. Coupling Spectroscopic Ellipsometry and Quartz Crystal Microbalance to Study Organic Films at the Solid–Liquid Interface. *Springer Series in Surface Sciences* **52**, 391–417 (2018).
31. Mataji-Kojouri, A., Ozen, M. O., Shahabadi, M., Inci, F. & Demirci, U. Entangled Nanoplasmonic Cavities for Estimating Thickness of Surface-Adsorbed Layers. *ACS Nano* **14**, 8518–8527 (2020).
32. Liu, A., Peng, J. & Li, G. Characterizing penetration depths of multi-wavelength surface plasmon resonance sensor using silica beads. *Applied Physics Letters* **104**, 211103 (2014).
33. Rupert, D. L. M. *et al.* Dual-Wavelength Surface Plasmon Resonance for Determining the Size and Concentration of Sub-Populations of Extracellular Vesicles. *Analytical Chemistry* **88**, 9980–9988 (2016).
34. Jung, L. S., Campbell, C. T., Chinowsky, T. M., Mar, M. N. & Yee, S. S. Quantitative interpretation of the response of surface plasmon resonance sensors to adsorbed films. *Langmuir* **14**, 5636–5648

- (1998).
35. Bohren, C. F. & Huffman, D. R. *Absorption and Scattering of Light by Small Particles*. (Wiley-VCH, 2007). doi:10.1002/9783527618156.
 36. Liu, N., Hentschel, M., Weiss, T., Alivisatos, A. P. & Giessen, H. Three-dimensional plasmon rulers. *Science* **332**, 1407–1410 (2011).
 37. Chen, W., Zhang, S., Deng, Q. & Xu, H. Probing of sub-picometer vertical differential resolutions using cavity plasmons. *Nature Communications* **9**, 801 (2018).
 38. Sönnichsen, C., Reinhard, B. M., Liphardt, J. & Alivisatos, A. P. A molecular ruler based on plasmon coupling of single gold and silver nanoparticles. *Nature Biotechnology* **23**, 741–745 (2005).
 39. Ferhan, A. R. *et al.* Nanoplasmonic Ruler for Measuring Separation Distance between Supported Lipid Bilayers and Oxide Surfaces. *Analytical Chemistry* **90**, 12503–12511 (2018).
 40. Jackman, J. A. *et al.* Quantitative profiling of nanoscale liposome deformation by a localized surface plasmon resonance sensor. *Analytical Chemistry* **89**, 1102–1109 (2017).
 41. Jackman, J. A. *et al.* Nanoplasmonic ruler to measure lipid vesicle deformation. *Chemical Communications* **52**, 76–79 (2016).
 42. Ferhan, A. R. *et al.* Nanoplasmonic Sensing Architectures for Decoding Membrane Curvature-Dependent Biomacromolecular Interactions. *Analytical Chemistry* **90**, 7458–7466 (2018).
 43. Jackman, J. A., Zhdanov, V. P. & Cho, N.-J. Nanoplasmonic Biosensing for Soft Matter Adsorption: Kinetics of Lipid Vesicle Attachment and Shape Deformation. *Langmuir* **30**, 9494–9503 (2014).
 44. Park, H. *et al.* Unraveling How Multivalency Triggers Shape Deformation of Sub-100 nm Lipid Vesicles. *The Journal of Physical Chemistry Letters* **12**, 6722–6729 (2021).
 45. Yoon, B. K., Park, H., Zhdanov, V. P., Jackman, J. A. & Cho, N. J. Real-time nanoplasmonic sensing of three-dimensional morphological changes in a supported lipid bilayer and antimicrobial testing applications. *Biosensors and Bioelectronics* **174**, 112768 (2021).
 46. Larsson, E. M., Edvardsson, M. E. M., Langhammer, C., Zorić, I. & Kasemo, B. A combined nanoplasmonic and electrodeless quartz crystal microbalance setup. *Review of Scientific Instruments* **80**, 125105 (2009).
 47. Chong, C. S. & Colbow, K. Light scattering and turbidity measurements on lipid vesicles. *Biochimica et Biophysica Acta (BBA) - Biomembranes* **436**, 260–282 (1976).
 48. Mazzotta, F. *et al.* Influence of the evanescent field decay length on the sensitivity of plasmonic nanodisks and nanoholes. *ACS Photonics* **2**, 256–262 (2015).
 49. Nugroho, F. A. A., Albinsson, D., Antosiewicz, T. J. & Langhammer, C. Plasmonic Metasurface for Spatially Resolved Optical Sensing in Three Dimensions. *ACS Nano* **14**, 2345–2353 (2020).
 50. Li, J. *et al.* Revisiting the Surface Sensitivity of Nanoplasmonic Biosensors. *ACS Photonics* **2**, 425–431 (2015).
 51. Kedem, O., Tesler, A. B., Vaskevich, A. & Rubinstein, I. Sensitivity and Optimization of Localized Surface Plasmon Resonance Transducers. *ACS Nano* **5**, 748–760 (2011).

52. Mayer, K. M. & Hafner, J. H. Localized surface plasmon resonance sensors. *Chemical Reviews* **111**, 3828–3857 (2011).
53. Murphy, C. J., Ardy Nugroho, F. A., Härelind, H., Hellberg, L. & Langhammer, C. Plasmonic Temperature-Programmed Desorption. *Nano Letters* **21**, 353–359 (2021).
54. Fredriksson, H. *et al.* Hole–Mask Colloidal Lithography. *Advanced Materials* **19**, 4297–4302 (2007).
55. Preston, A. S., Hughes, R. A., Demille, T. B. & Neretina, S. Plasmonics under Attack: Protecting Copper Nanostructures from Harsh Environments. *Chemistry of Materials* **32**, 6788–6799 (2020).
56. Preston, A. S., Hughes, R. A., Dominique, N. L., Camden, J. P. & Neretina, S. Stabilization of Plasmonic Silver Nanostructures with Ultrathin Oxide Coatings Formed Using Atomic Layer Deposition. *The Journal of Physical Chemistry C* **125**, 17212–17220 (2021).
57. Nugroho, F. A. A. *et al.* Plasmonic Nanospectroscopy for Thermal Analysis of Organic Semiconductor Thin Films. *Analytical Chemistry* **89**, 2575–2582 (2017).
58. Kvasnička, P. & Homola, J. Optical sensors based on spectroscopy of localized surface plasmons on metallic nanoparticles: Sensitivity considerations. *Biointerphases* **3**, FD4–FD11 (2008).
59. Miller, M. M. & Lazarides, A. A. Sensitivity of metal nanoparticle surface plasmon resonance to the dielectric environment. *Journal of Physical Chemistry B* **109**, 21556–21565 (2005).
60. Frost, R. *et al.* Core–Shell Nanoplasmonic Sensing for Characterization of Biocorona Formation and Nanoparticle Surface Interactions. *ACS Sensors* **1**, 798–806 (2016).
61. Jonsson, M. P., Jönsson, P. & Höök, F. Simultaneous nanoplasmonic and quartz crystal microbalance sensing: Analysis of biomolecular conformational changes and quantification of the bound molecular mass. *Analytical Chemistry* **80**, 7988–7995 (2008).
62. Nugroho, F. A. A. *et al.* Topographically Flat Nanoplasmonic Sensor Chips for Biosensing and Materials Science. *ACS Sensors* **2**, 119–127 (2017).
63. Dave, P. C., Tiburu, E. K., Damodaran, K. & Lorigan, G. A. Investigating Structural Changes in the Lipid Bilayer upon Insertion of the Transmembrane Domain of the Membrane-Bound Protein Phospholamban Utilizing ³¹P and ²H Solid-State NMR Spectroscopy. *Biophysical Journal* **86**, 1564–1573 (2004).
64. Huber, T., Rajamoorthi, K., Kurze, V. F., Beyer, K. & Brown, M. F. Structure of docosahexaenoic acid-containing phospholipid bilayers as studied by ²H NMR and molecular dynamics simulations. *Journal of the American Chemical Society* **124**, 298–309 (2002).
65. Brunauer, S., Emmett, P. H. & Teller, E. Adsorption of Gases in Multimolecular Layers. *Journal of the American Chemical Society* **60**, 309–319 (1938).
66. Klobes, P. M. K.; M. R. G. *Porosity and Specific Surface Area Measurements for Solid Materials*. https://tsapps.nist.gov/publication/get_pdf.cfm?pub_id=854263 (2006).
67. Mapar, M. *et al.* Spatiotemporal Kinetics of Supported Lipid Bilayer Formation on Glass via Vesicle Adsorption and Rupture. *Journal of Physical Chemistry Letters* **9**, 5143–5149 (2018).

68. Keller, C. A., Glasmästar, K., Zhdanov, V. P. & Kasemo, B. Formation of Supported Membranes from Vesicles. *Physical Review Letters* **84**, 5443 (2000).
69. Richter, R. P., Bérat, R. & Brisson, A. R. Formation of solid-supported lipid bilayers: An integrated view. *Langmuir* **22**, 3497–3505 (2006).
70. Zhdanov, V. P., Keller, C. A., Glasmästar, K. & Kasemo, B. Simulation of adsorption kinetics of lipid vesicles. *The Journal of Chemical Physics* **112**, 900 (1999).
71. Jose, J. *et al.* Topographically flat substrates with embedded nanoplasmonic devices for biosensing. *Advanced Functional Materials* **23**, 2812–2820 (2013).
72. Li, K. *et al.* Extended Kalman Filtering Projection Method to Reduce the 3σ Noise Value of Optical Biosensors. *ACS Sensors* **5**, 3474–3482 (2020).
73. Nugroho, F. A. A. *et al.* Metal–polymer hybrid nanomaterials for plasmonic ultrafast hydrogen detection. *Nature Materials* **18**, 489–495 (2019).
74. Johnson, P. B. & Christy, R. W. Optical constants of the noble metals. *Physical Review B* **6**, 4370–4379 (1972).

Figures

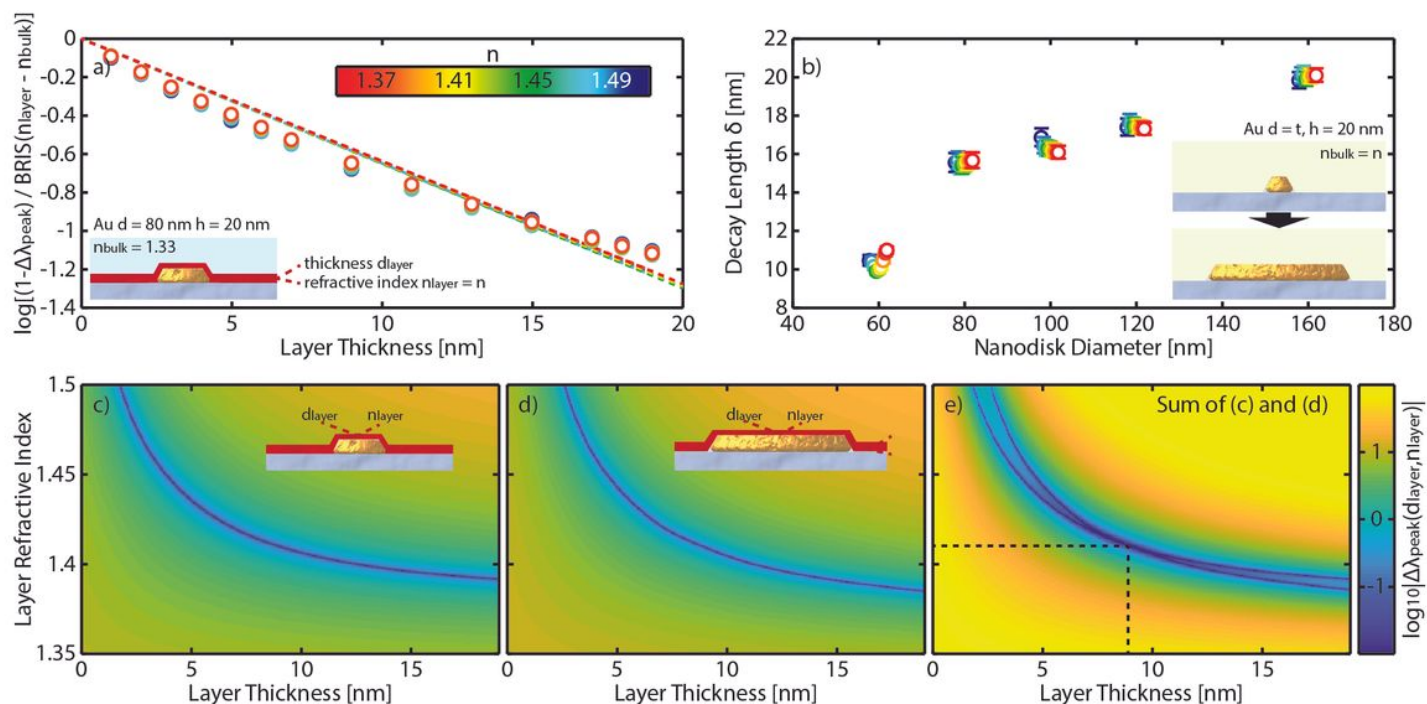


Figure 1

Design consideration for a dual-band nanoplasmonic ruler. (a) FDTD-calculated $\Delta\lambda_{peak}$ of a Au nanodisk in water covered with thin conformal layers of up to 20 nm thickness and with RI of 1.35 to 1.5, expressed as Eq. 8, as a function of the layer thickness (the data points are presented by using BRIS calculated in Supplementary Figure 1, which is used as a fitting parameter). The dashed lines are the exponential

approximation of the LSPR sensitivity, in which the linearity confirms that the SPR model is a good approximation for the inhomogeneous fields in a nanodisk, whose effective decay length, δ , is given by the inverse slope of the dashed lines. The inset shows a to-scale schematic of the simulated system. (b) The effective decay lengths, δ , for nanodisks of 20 nm height and varying diameter in a medium of different RI. Error bars represent the confidence intervals of the linear regression when fitting the logarithm of the exponential function in Eq. 8. (c,d) $\Delta\lambda_{peak}$ of a nanoplasmonic sensor comprising a Au nanodisk of height 20 nm and (c) 80 nm and (d) 160 nm diameter, coated with a conformal dielectric layer with various thickness, d_{layer} and RI, n_{layer} subtracted by $\Delta\lambda_{peak}$ of the corresponding sensors when d_{layer} and n_{layer} are 9 nm and 1.41, respectively. It is clear that knowing only $\Delta\lambda_{peak}$ it is impossible to deduce d_{layer} and n_{layer} as there are infinite combination possibilities that result in a similar $\Delta\lambda_{peak}$ compared to when the surface is covered with a layer of 9 nm with RI of 1.41. (e) Combining the two independent results of (c) and (d) enables unambiguous determination of both d_{layer} and n_{layer} i.e., 9 nm and 1.41, respectively (dashed lines).

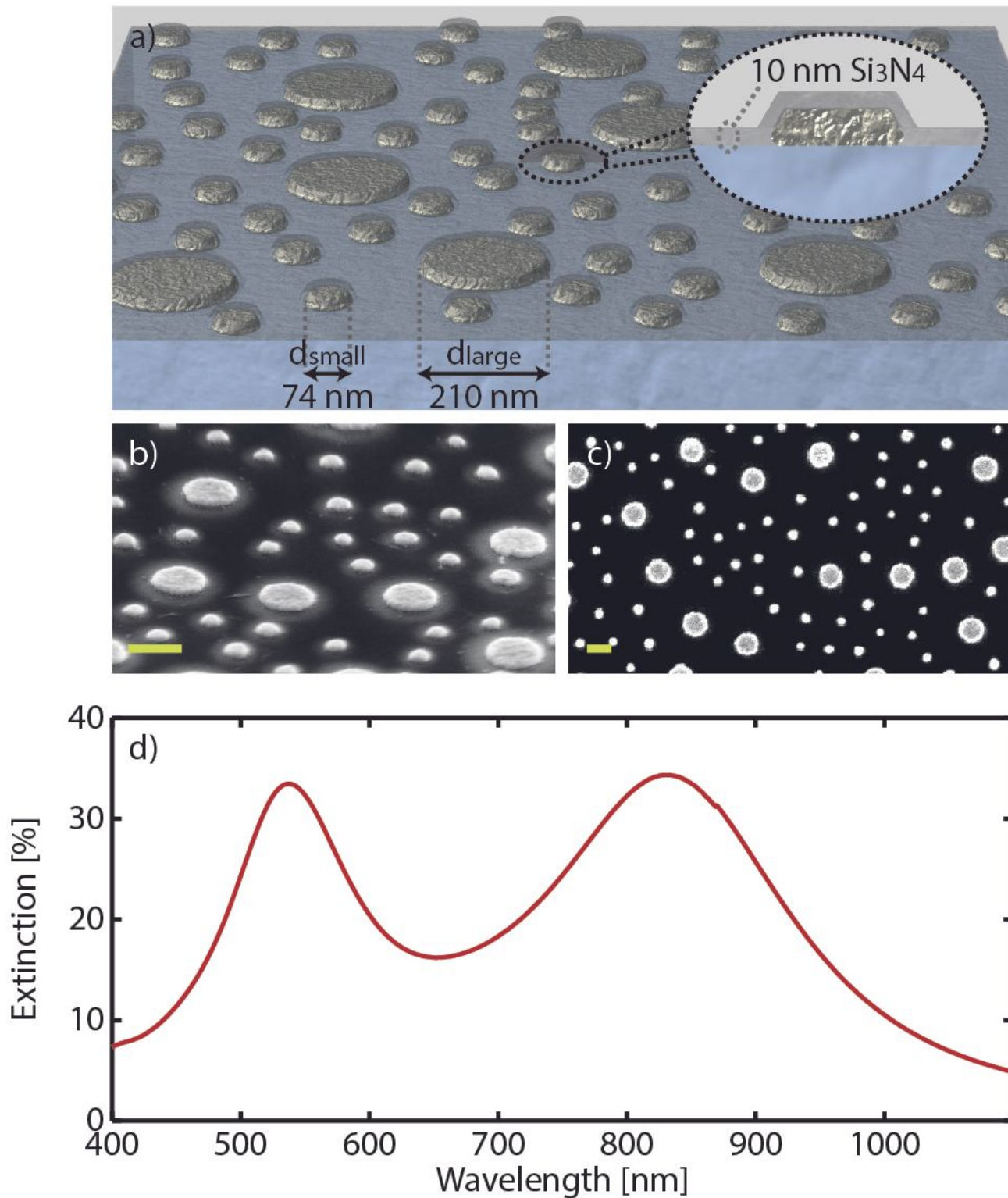


Figure 2

Dual-band nanoplasmonic ruler design and optical spectra. (a) Artist's rendition of the sensor surface comprising a quasi-random array of two distinct populations of Ag nanodisks with diameters $d_{\text{small}} = 74 \text{ nm}$ and $d_{\text{large}} = 210 \text{ nm}$, both with a height $h = 20 \text{ nm}$ and covered with a conformal 10 nm thin Si_3N_4 coating (inset). (b) Tilted and (c) normal incidence SEM images of the corresponding nanostructured surface. Note that the imaged sensor is not coated with Si_3N_4 for better image contrast. Scale bars are

200 nm. (d) Optical extinction spectra of the dual-band nanoplasmonic ruler sensor characterized by two spectrally distinctly separated peaks with identical intensity.

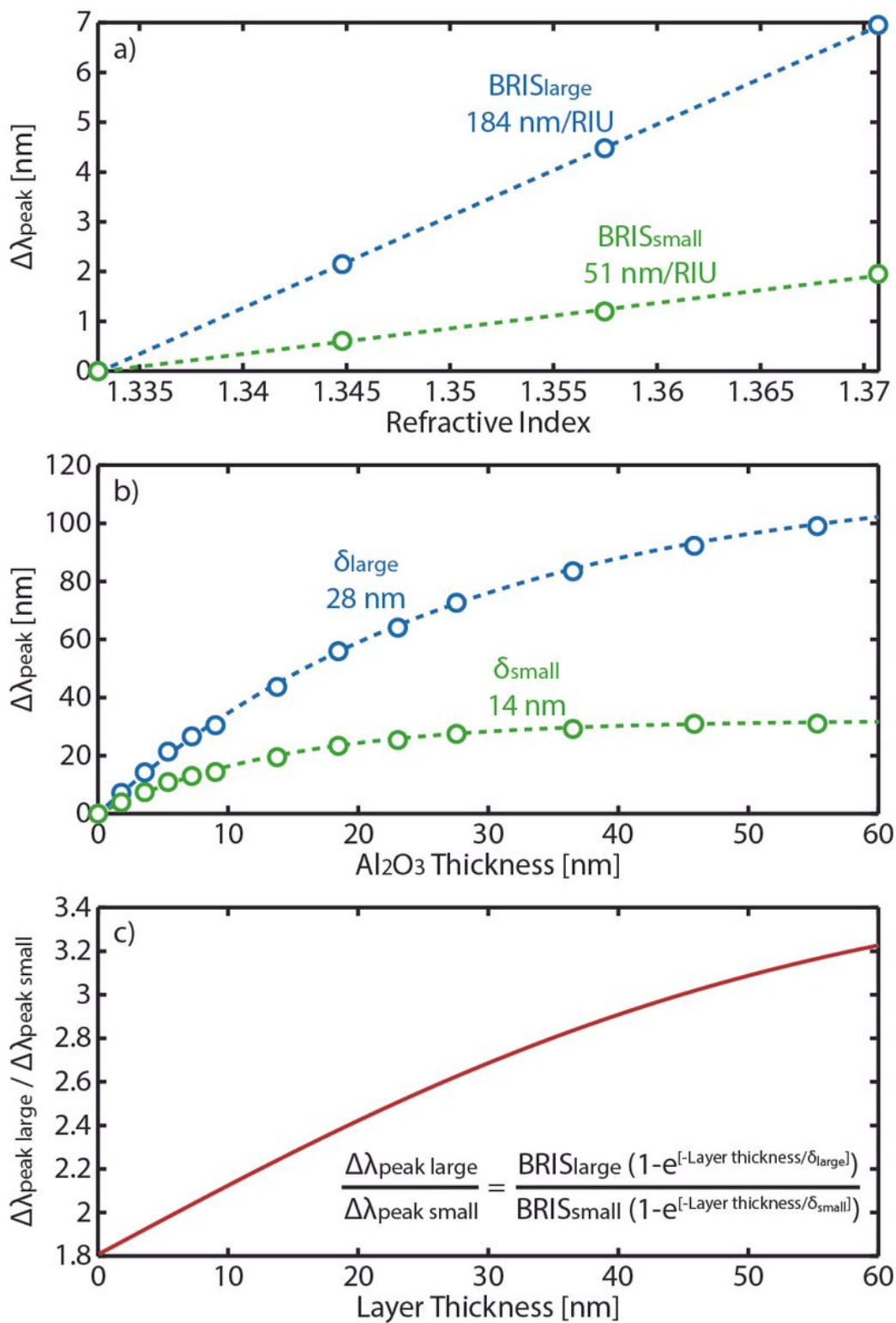


Figure 3

Sensitivity, field decay length determination and sensor-response-to-layer-thickness conversion plot of the dual-band nanoplasmonic ruler. (a). Bulk refractive index sensitivity, BRIS, and (b) decay length, δ ,

determination for the small and large nanodisks in the mixed array. Dashed lines in (a) and (b) are linear fits and a fit of the data to Eq. 4,^{34,49} respectively. (c) Nanoruler conversion plot which translates the $\Delta\lambda_{peak}$ ratio of the large and small nanodisks into the (cumulative) thickness of the layer on top of the sensor.

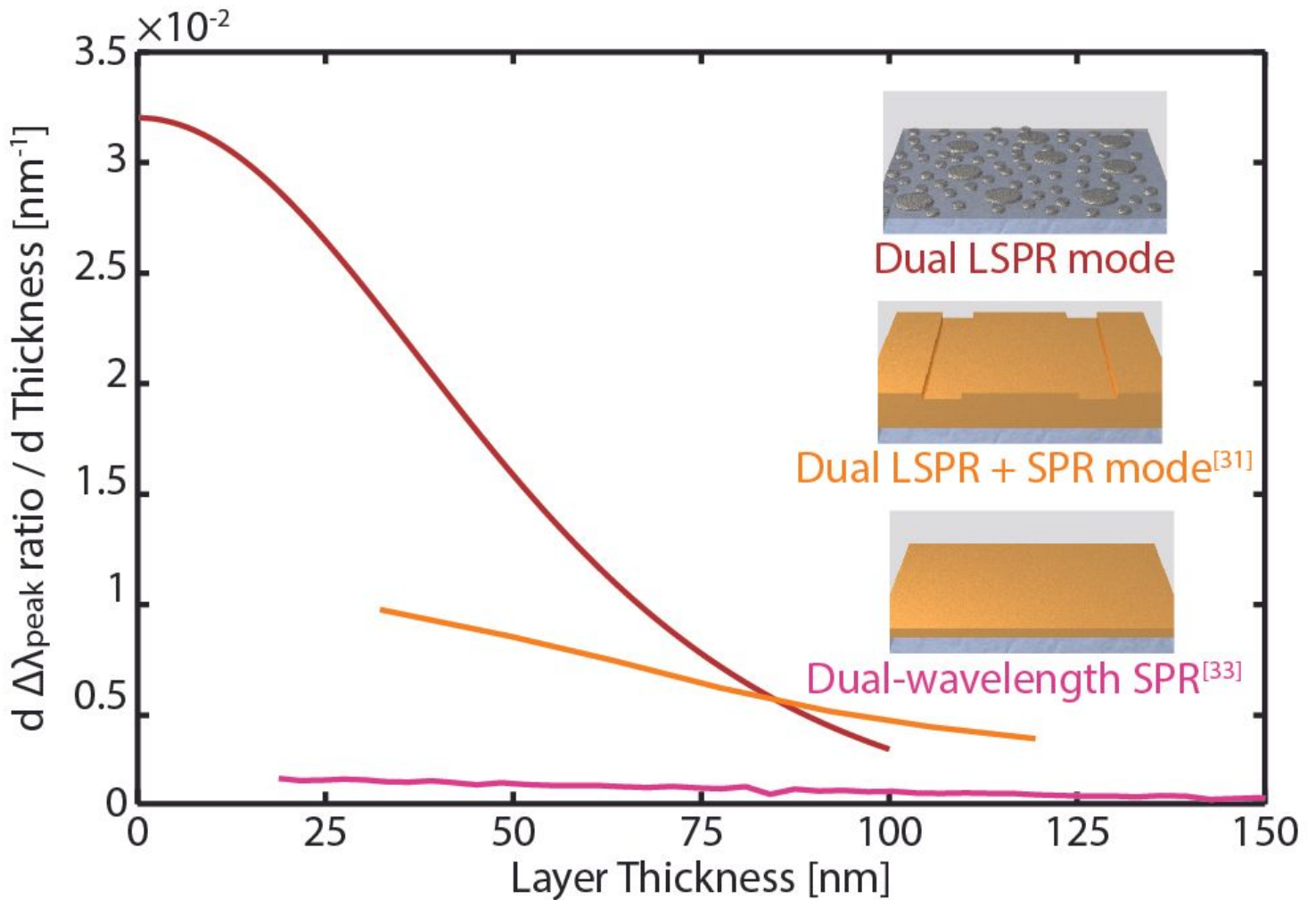


Figure 4

Dual-band plasmonic nanoruler sensitivity. The derivative of the conversion plot (cf. Fig. 3c) reveals the sensitivity of the nanoruler, i.e., the change in the absolute $\Delta\lambda_{peak}$ ratio per 1 nm change of the layer thickness. The triple sensitivity at a layer thickness up to ~ 20 nm compared to those beyond ~ 50 nm stems from the characteristic high local sensitivity of LSPR sensors, which is a consequence of the rapidly decaying near fields. The overall sensitivity of our dual-mode LSPR nanoruler in the few tens of nanometer thickness range is therefore at least twice as high as for LSPR-SPR mode³¹ and dual SPR mode³³ solutions.

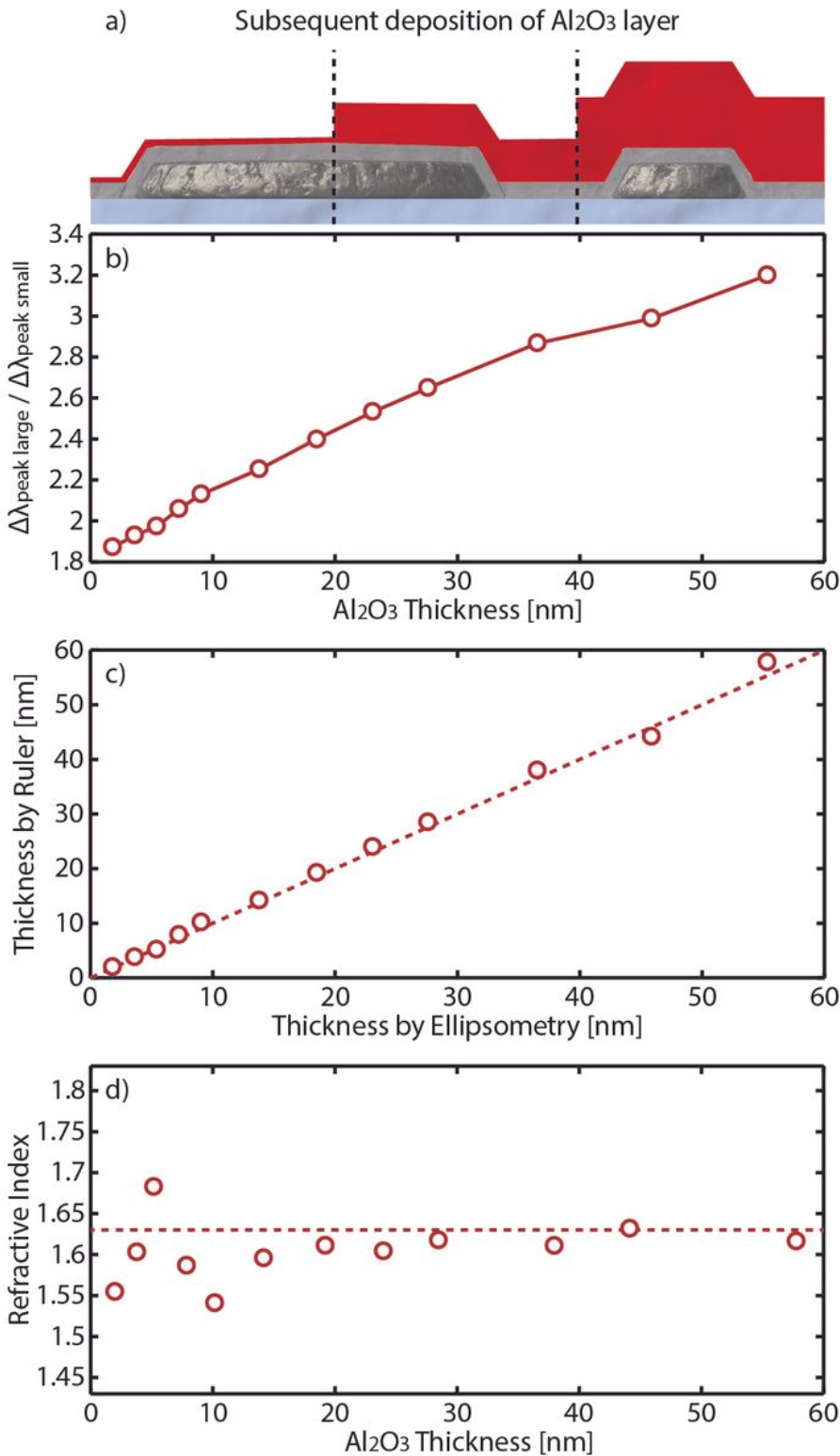


Figure 5

Measuring cumulative layer thickness and RI in air. (a) Schematic of the studied system comprising a gradual build-up of thin Al₂O₃ layers. (b) The corresponding $\Delta\lambda_{\text{peak}}$ ratio of the large and small nanodisks. (c) The comparison between the layer thicknesses derived with the nanoruler (i.e., by translating the $\Delta\lambda_{\text{peak}}$ ratio to layer thickness through the conversion plot in **Fig. 3c**) and using ellipsometry. The thickness determination by the nanoruler up to 60 nm is in excellent agreement with the

values obtained by ellipsometry. Dashed line is the one-to-one relation between the abscissa and the ordinate. (d) The corresponding RI determination of the accumulated thin Al_2O_3 layers. Dashed line is the corresponding RI measured by ellipsometry.

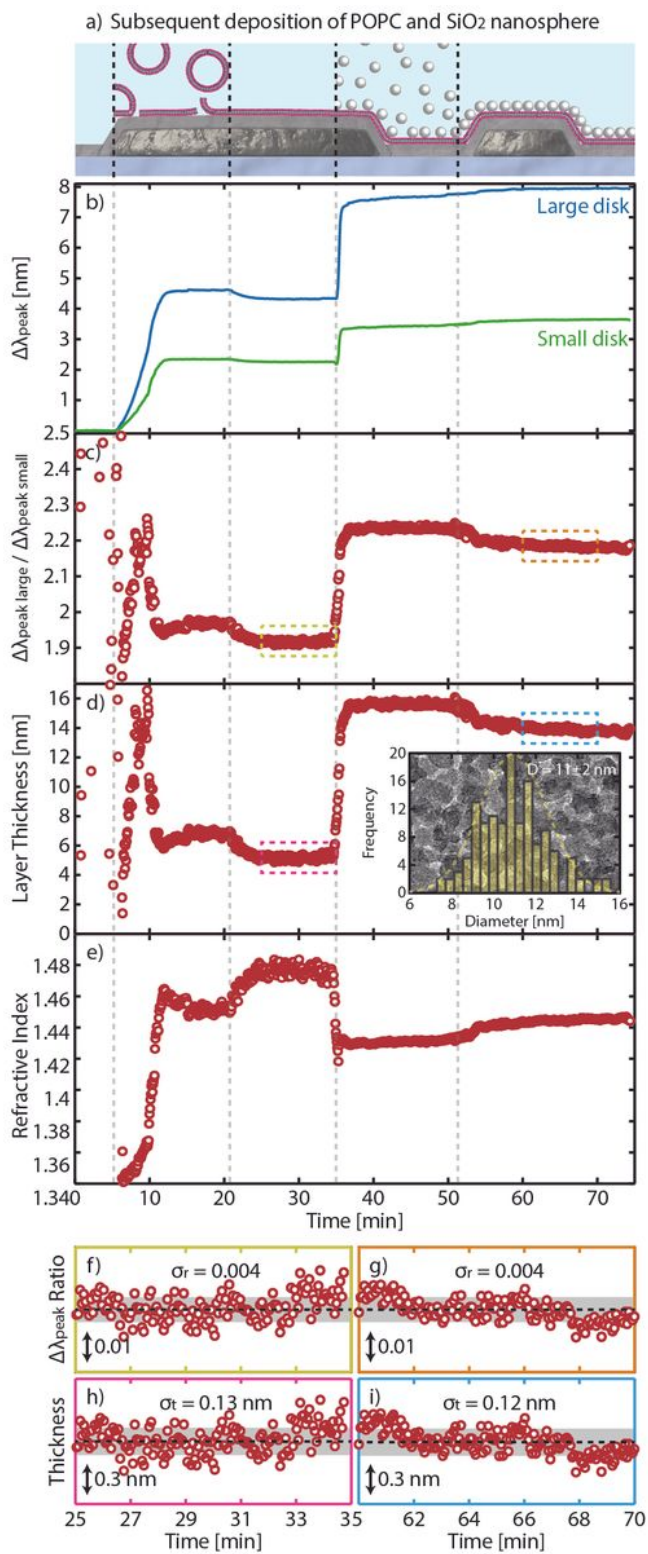


Figure 6

Measuring two different layers in liquid medium. (a) Schematic of the studied system and its various deposition phases: starting from a bare sensor, we deposit POPC vesicles that eventually rupture and form a supported lipid bilayer (SLB), onto which we adsorb SiO_2 nanospheres that form a monolayer after rinsing. Note that the vesicles, SLB, and the SiO_2 nanospheres are drawn to-scale to the Au nanodisk dimensions, while the binding conformations are arbitrary and should only serve as schematic conceptual illustration. (b) The corresponding temporal evolution of the $\Delta\lambda_{\text{peak}}$ of small and large nanodisks, showing markedly different response as the deposition phase progresses, as delineated by the dashed lines. (c) The $\Delta\lambda_{\text{peak}}$ ratio of the small and large nanodisks. (d) The real-time layer(s') thickness determined by the nanoruler, showing the drastic thickness change prior to the SLB formation and subsequent thickness increase after the addition of the SiO_2 nanospheres. Inset: size distribution histogram of SiO_2 nanospheres derived via TEM image analysis, with a representative dark-field TEM image in the background. The image is $120 \times 80 \text{ nm}^2$. (e) The real-time layer(s') RI determined by the nanoruler. (f,g) Zoom-in version of panels (c) and (d) showing the typical $\Delta\lambda_{\text{peak}}$ ratio and derived thickness, respectively, at two different occurrences in the experiment. Assessing the noise, it is clear that it is constant throughout the experiment and is small, i.e., $\sigma_r = 0.004$ and $\sigma_t = 0.13 \text{ nm}$ for the $\Delta\lambda_{\text{peak}}$ ratio and thickness determination, respectively. Defining the limit of detection as $3\sigma_t$, the nanoruler is able to distinguish a 0.5 nm thickness difference for total layer thickness up to 60 nm (cf. **Fig. 3c**).

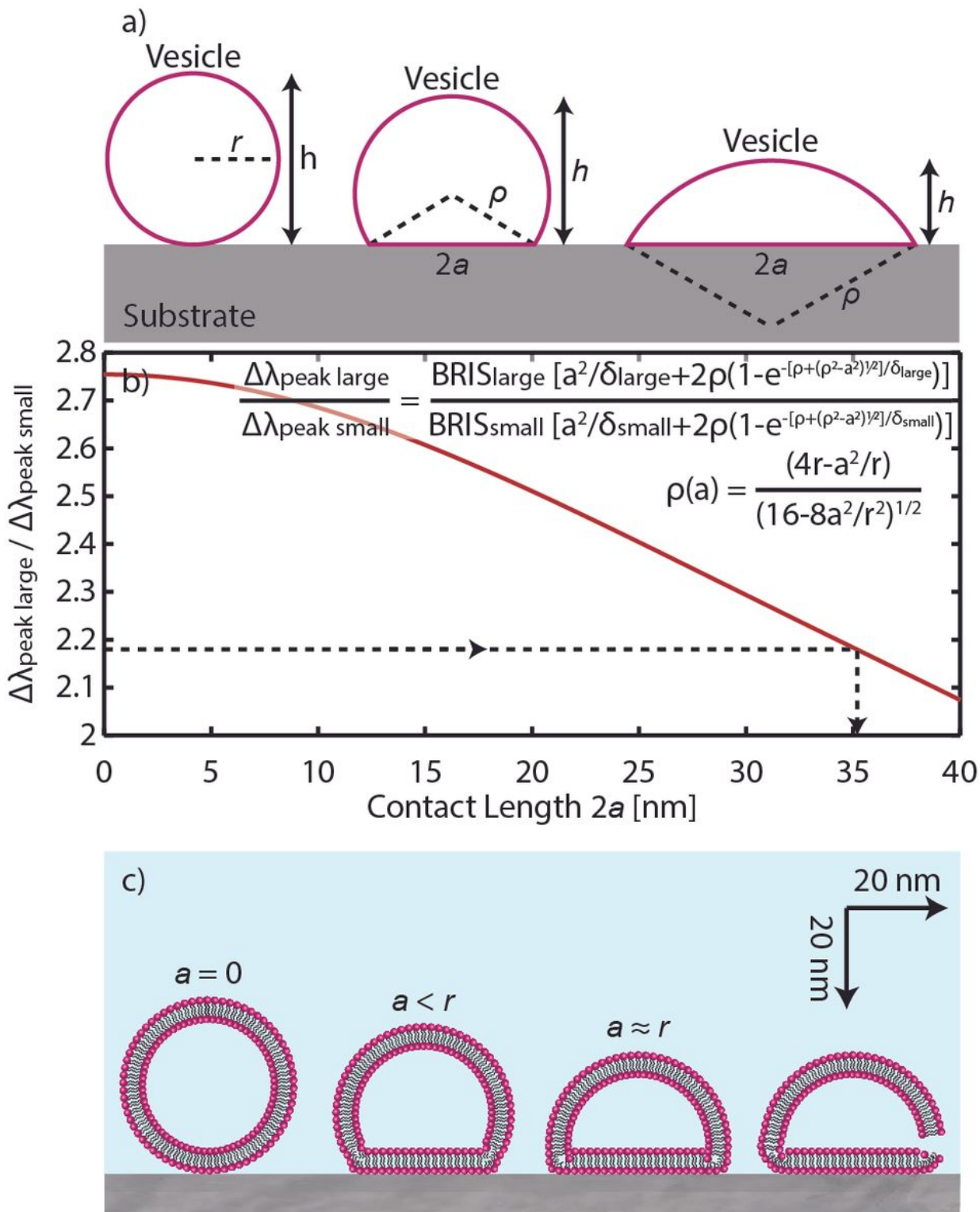


Figure 7

Quantifying the deformation degree of vesicles prior to rupture and SLB formation. (a) Definition of the parameters used to quantify the deformation of an adsorbed vesicle which is represented by a truncated sphere with the assumption that its surface area is preserved. r is the radius of an intact vesicle, h is the vesicle height, ρ is the radius of a deformed vesicle, and a is the radius of the vesicle-support contact region. (b) Nanoruler conversion plot which translates the $\Delta\lambda_{\text{peak}}$ ratio of the large and small nanodisks

(according to Eq. 12) into the contact length $2a$ of the deformed vesicles on top of the sensor. Translating the $\Delta\lambda_{peak}$ ratio at the onset of rupture (i.e., $\Delta\lambda_{peak}$ ratio of 2.18, cf. **Fig. 6c**) to $2a$, results in critical contact length of 35.4 nm (dashed line), that is comparable to the initial vesicle diameter. (c) To-scale schematic of the adsorption and rupture processes of the studied vesicle. The vesicle adsorbs on the support and relaxes until the contact length becomes close to its initial diameter and rupture is initiated provided the vesicle coverage becomes equal to or is slightly above the critical one.

Supplementary Files

This is a list of supplementary files associated with this preprint. Click to download.

- [NugrohoetalSI.docx](#)